ARTICLE

Local Synergetic Collaboration between Pd and local tetrahedral symmetric Ni Oxide enables ultra-high-performance CO_2 Thermal Methanation

Che Yan,[a] Chia-Hsin Wang,[b*] Moore Lin,[c] Dinesh Bhalothia,[a] Shou-Shiun Yang,[a] Gang-Jei Fan,[c] Jia-Lin Wang,[c] Ting-Shan Chan,[b] Yao-lin Wang,[d] Xin Tu,[d] Sheng Dai,[e] Kuan-Wen Wang,[f] Jr-Hau He,[g] and Tsan-Yao Chen[a, h, i*]

A hierarchically structured bimetallic nanocatalyst (NC) comprising a metallic Pd-nanocluster adjacent to local tetrahedral symmetric Ni-oxide and a thin layer of Tetramethyl orthosilicate (TMOS) decoration (denoted as NiO_TPd-T) is synthesized by sequential control of the metal ion adsorption followed by the wet chemical reduction on the carbon nanotube support. By cross-referencing results of physical structure inspections, in-situ ambient pressure X-ray photoelectron spectroscopy, and gas chromatography-mass spectrometer analysis, we demonstrate that the NiO_TPd-T gains the optimum production yield of 1905.1 mmol/g on CH_4 and is more than 10-fold improved as compared to that of TMOS decorated Pd nanocatalysts (Pd-T) at 573 K. Such an exceptional performance is attributed to the local synergetic collaboration between CO chemisorption on Pd atoms and H_2 splitting on both Pd and Ni atoms at the interface region. Once the collaboration is triggered, the subsequent NiO_T reduction increases the amount of metallic Ni sites. It further facilitates the H_2 splitting, therefore, optimizing the CH_4 production yield of NiO_TPd-T. Most importantly, to the best of our knowledge, with such a unique Pd-to-NiO_T epitaxial structure, the NiO_TPd-T catalysts exhibit the highest CH_4 production yield among existing catalysts with the same loading, composition, and any geometric configurations.

Introduction

With the rising energy demand and climate disorders, development of techniques for converting unstable renewable energy to chemical forms simultaneously restoring the carbon emission is an inevitable task for the sustainability of modern society. Regardless of any technology been developed for suppressing carboxyl pollutant, CO_2 "which is one of the most influential greenhouse gas" emission is the thorniest problem that leading to the thermal runaway on earth and is no way to elude. Reducing CO_2 and turning it to valuable fuels (e.g. hydrocarbon, methane, etc.) by waste heat or inconstant electricity is an ideal strategy fulfil the aforementioned scenarios.[1] Among existing methods, the thermal reduction of CO_2 is one of the promising techniques for restoring waste heat in terms of cost and facile considerations. Such a method can be adapted to the state-of-the-art industrial facilities without additional efforts for collecting the carbon and heat sources. However, due to the high threshold temperature, the existing materials and system designs make the CO_2 reduction reaction (CO_2RR) far from practical applications. Heterogeneous catalysis is a potential strategy for simultaneously reducing the threshold temperature and enhancing the production yield of the CO_2RR.[2] By tuning the configuration and composition, four reaction mechanisms including dimension - shape effects, bifunctional mechanism, ligand effect, and lattice strain involved, however, the collaboration between reaction sites seldom been reported in the CO_2RR pathways on the NC surface.

There are four typical catalysis reaction for converting CO_2 to various chemicals including dry reforming of methane ($CH_4 + CO_2 \rightarrow 2CO + 2H_2$), CO_2 methanation ($CO_2 + 4H_2 \rightarrow CH_4 + 2H_2O$), and CO productions.[3-6] Among them, CO_2 methanation is considered as the most important technique since it can be triggered by the waste heat of combustion engines. By adopting proper collection facilities, the end products can be

a. Department of Engineering and System Science, National Tsing Hua University, Hsinchu 30013, Taiwan. T.-Y. Chen Email: chencaeser@gmail.com; Tel: +886-3-5715131#34271
b. National Synchrotron Radiation Research Center, Hsinchu 30076, Taiwan
c. Department of Chemistry, National Central University, Taoyuan 32001, Taiwan
d. Department of Electrical Engineering and Electronics, University of Liverpool, Liverpool L69 3GJ, UK
e. School of Chemistry & Molecular Engineering, East China University of Science and Technology, Shanghai 200237, P.R. China
f. Institute of Materials Science and Engineering, National Central University, Taoyuan City 32001, Taiwan.
g. Department of Materials Science and Engineering, City University of Hong Kong, Hong Kong
h. Institute of Nuclear Engineering and Science, National Tsing Hua University, Hsinchu 30013, Taiwan
i. Hierarchical Green-Energy Materials (Hi-GEM) Research Centre, National Cheng Kung University, Tainan 70101, Taiwan
Electronic Supplementary Information (ESI) available: [details of any supplementary information available should be included here]. See DOI: 10.1039/x0xx00000x

redistributed to the core units and thus greatly improve the energy efficiency of a power machine. Firepower plant (which emits the largest amount of waste heat and CO_2 among all mechanical units) is an important target for adopting the CO_2RR. In such a high-power density system, the temperature of waste heat in the steam passing through the turbine is ~600 °C.[7] From thermodynamic theory, the optimum energy efficiency of the turbine generator is ~47% meaning that a substantial waste heat emission is inevitable and should be properly managed. Adopting heterogeneous NCs in CO_2RR is an effective assessment for the waste heat management in the meantime reducing the carbon emission. With proper configuration and composition designs, the methanation reaction of heterogeneous NCs possesses an optimum conversion efficiency of CO_2 (99.2 %) at the temperature ranging from 250 °C to 400 °C and with a CH_4 selectivity higher than 90%.[2, 8-14] Ni-based NCs with oxide support are commonly employed as catalysts for the thermal methanation. In such a NC, the oxide support plays two important roles in CO_2RR including (i) nucleation and growth sites of uniform dispersed nanoparticles (e.g. surface activated Al_2O_3, SiO_2 and TiO_2)[14-15] and (ii) a carbon adsorption carrier with high mobility of oxygen ions (e.g. CeO_2 and ZrO_2).[4, 16, 17] These two factors improve the selectivity and reaction kinetics of CO_2RR, respectively. Transition metals of group VIIIB (Fe, Co, Ni, Ru, Pd, Pt) were conventionally introduced to the CO_2 methanation.[18] Among them, Ni-based materials are most likely one of the best potential candidates for the industrial operation in terms of both cost and performance considerations.[5] A famous example was conducted by Tan, J. J. and his collaborators who hit a striking selectivity of nearly 100% in CH_4 by using the MgO doped Ni/ZrO_2 NCs at 250 °C.[5] However, only a few groups reach a high production yield on the CH_4.[1, 18] To do this, Bermejo-Lopez, A., et al employed the wet impregnation method to synthesize a co-catalyst comprising 4% of Ru and 10% of Na_2CO_3/Al_2O_3 NCs. In this NCs, the Na_2CO_3 not only facilitates the Ru dispersion but served as the active sites for CO_2 absorption. Such a design enables the collaboration between metallic NC and surrounding reaction sites, therefore, facilitates the reaction kinetics of CO_2RR. However, the low stability of carbonates suppresses both the performance and operational lifetime of such type of NC in CO_2RR at high temperature.[18]

To reinforce the production yield and suppress the degradation effects in CO_2RR, the novel concept of local synergetic collaboration in heterogeneous NCs is proposed in this study. For elucidating the details, a bimetallic NC comprising an epitaxial structure of Pd nanocrystal adjacent to the Ni-oxide with a tetrahedral symmetry in local structure and covered by a thin layer of Tetramethyl orthosilicate (TMOS) decoration (denoted as NiO_TPd-T) is developed. To the best of our knowledge, the epitaxial structured NC (i.e. NiO_TPd-T) in this study exhibits the highest reported CH_4 production yield when compared to the bimetallic NCs in the similar compositions and components at a temperature below 600K (**Table S1**). In the experimental NiO_TPd-T, the collaboration between NiO_T and Pd interface triggers the methanation at a near-room temperature (323 K) in a considerable amount (0.4 mmol/g) and hit an impressive CH_4 production yield to 1905.1 mmol/g with a high concentration of CO_2 (75%) at 573 K. The corresponding mechanisms of the local synergetic collaboration between NiO_T and metallic Pd nanocrystal are schematically revealed by cross-referencing the results of static physical structure inspections, in-situ ambient pressure X-ray photoelectron spectroscopy (in-situ APXPS), and gas chromatography-mass spectrometer (GC-MS) analysis. In brief, herein we proposed a novel prospectus on CO_2 thermal methanations with reconcilable balance between catalytic activity and cost considerations.

Experimental

Synthesis of CNT supported NiO_TPd-T Bimetallic NC

The heterogeneous catalyst comprising an epitaxial structure of metallic Pd-to-NiO_T nanocrystal with the surface decoration of TMOS was synthesized by sequential chemisorption followed by reduction of Ni and Pd metal ions on carbon nanotube (CNT) surface. To enhance the attachment of catalysts on the support material, carbon nanotubes (CNTs, 5.0 wt.% Cnano Technology Ltd.) were acid-treated by an aqueous solution of sulfuric acid (6.0 M) at 70 °C for 4h, filtered and then washed with distilled water till pH value >5. In the first step, 500.0 mg of acid-treated CNTs (A-CNTs) were dispersed in 1.28 g of aqueous solution of nickel (II) chloride hexahydrate (0.1 M) ($NiCl_2•6H_2O$, Showa chemical Co. Ltd.) solution and stirred at 200 rpm at 70 °C for 4 h (solution denoted S1). In this solution, the metal loading of Ni to A-CNT is 30 wt.%. In the second step, 5.0 ml of an aqueous solution containing 57.9 mg of $NaBH_4$ (99%, Sigma-Aldrich Co.) is added to S1 for 10 seconds. In this step, metastable Ni-oxide nanoparticles were formed (NiO_T/A-CNT sample). In the third step, 1.92 g of Pd precursor solution (0.1 M) was added to NiO_T/A-CNT sample. In this step, Pd ions were reduced and deposited on the NiO_T surfaces (namely NiO_TPd) by interacting with the excessive amount of $NaBH_4$ added in step 2. The Pd precursor solution was prepared by dissolving palladium (II) chloride ($PdCl_2$, 99%, Sigma-Aldrich Co.) in 1.0 M $HCl_{(aq)}$. The atomic ratio of Pd/Ni is 1.5 for NiO_TPd NCs. The samples are washed several times with acetone, centrifuged, and then dried at 70 °C. For decorating the thin TMOS layer, the dried powder of NiO_TPd NC was dispersed in a 30 ml of methanol containing 14.0 mg of Tetramethyl orthosilicate (Sigma-Aldrich 98%, TMOS) and stirred at a speed of 250 rpm for 4h. The sample is again washed, centrifuged, and then dried at 70 °C resulting in the NiO_TPd NC. Control samples (NiO_T-T and Pd-T), are synthesized by immersing Ni (Pd) precursor solution in A-CNT at 25 °C for 4 hours followed by adding reducing agent (0.023 mg of $NaBH_4$ in 5.0 ml H_2O) and repeating the steps of TMOS decoration. The metal loading of Ni (Pd)/A-CNT ratio is 30 wt.%.

Physical characterizations of Experimental NCs

The surface morphologies of as-prepared NCs were analyzed by using high angle annular dark field scanning transmission electron microscopy (HAADF-STEM) images, which were recorded using a convergence semi-angle of 22mrad and inner and outer collection angles of 83 and 165mrad, respectively.

The atomic distribution of NiO_TPd-T is determined by EDX mapping at the East China University of Science and Technology. High-resolution transmission electron microscopy (HRTEM) operated at a voltage of 200 kV in the Research Building of fundamental science education, Precision Instruments Center of Taiwan was used to find out the inter-planar distance of as-prepared NCs. The X-ray diffraction (XRD) patterns are measured with the incident X-ray of wavelength 0.6888 Å (18.0 keV) at beamline of BL-01C2 at National Synchrotron Radiation Research Center (NSRRC), Taiwan. Average coherent length of experimental NCs is calculated from XRD peak broadening of (111) facets using the Scherrer equation: [26]

$$D = \frac{0.94 \times \lambda}{\beta \times \cos\theta} \qquad (1a)$$

Where D is the crystal size of Pd, λ is the wavelength of x-ray (0.6889 Å), θ is the half diffraction angle of the peak and β is the true half peak width. The XAS spectra of the experimental NCs were measured in the fluorescence mode at the beamlines BL01C1 and 17C of NSRRC (Taiwan). A Si monochromator was employed to adequately select the energy with a resolution $\Delta E/E$ better than 10^{-4} at the Pd K edge (24350 eV) and Ni K edge (8333 eV). All catalysts were dispersed uniformly on the tape and prepared as thin pellets with an appropriate absorption thickness ($\mu x = 1.0$, where μ is the X-ray attenuation coefficient at the absorption edge and x is the thickness of the sample) to attain a proper edge jump step at the absorption edge region. To acquire acceptable quality spectra with good quality, each measurement was repeated at least twice and averaged for successive comparison. For the EXAFS analysis, the backgrounds of the pre-edge and the post-edge were subtracted and normalized with respect to the edge jump step from the XAS spectra. The normalized spectra were transformed from energy to k-space and further weighted by k^3 to distinguish the contributions of backscattering interferences from different coordination shells. APXPS was carried out at the beamline BL24A of Taiwan light source (TLS) at the National Synchrotron Radiation Research Center (NSRRC). The samples were prepared in the form of pellets with a diameter of 5 mm by the hydraulic press and then inserted to powder cell holder.[27] The experimental conditions were separated into two parts when measuring the spectrum at a photon energy of 1000 eV for each step. In the first part, the sample was heated from RT to 573 K at 0.11 mbar carbon dioxide (CO_2) pressure. During which, the sample was kept at RT and high vacuum in the first step (denoted as **Vac**) and then purged by carbon dioxide at 0.11 mbar in the second step (denoted as **P1**). After data collection, the sample was heated by a CW laser beam shine at the back side of holder at the increment of each 50 K temperature as a step form 323 K to 573 K for spectra measurement. After the final step of the first part, the sample was naturally cooled down to RT in the chamber at high vacuum (denoted as **R-V**). In the second part, the sample was purged by a mixture of carbon dioxide and hydrogen (CO_2: H_2 = 1: 3) at 0.11 mbar (denoted as **P2**). Again, the sample was heated from 323 K to 573 K with an increment of 50K for spectra measurement. In the last step, the

system was naturally cooled to RT at high vacuum at 10^{-8} torr (denoted as **R-V2**).

Catalytic Activity Measurements

The standard gases including H_2 and CO (each 200 ppm), as well as CH_4, C_2H_6 and C_3H_8 (each 100 ppm) balanced in He were purchased from ECGAS Asia (Taiwan). To prepare different concentrations of these gases, it is carried out by introducing gases into sampling loops of various sizes. The gas cylinder was directly connected to the 6-port switching valve to fill the sampling loop which was then injected into the GC column. For the catalytic study, gas samples were directly collected from the thermal catalytic reactor. The experiment was performed with an automatic premixed gas supply apparatus equipped with a heating block for the chosen catalyst to be packed within a glass tube to form a thermal reaction bed. The glass tube packed with catalyst has a size of 100 mm in length, 2 mm for the inside diameter and 3 mm for the outside diameter (**Figure S5b**). The temperature of the reaction bed can be program-controlled by a thermal controller with PID algorithm. This apparatus allows users to set up an analytical method with the desired reaction time, temperature and flow rate, as well as to remote-start a GC with a self-designed software as the interface. The schematic diagram of the apparatus is shown in **Figure S5a**. The total flow rate of the gases is measured and controlled by a mass flow controller (MFC). All gaseous samples coming from the reaction bed are analyzed by a gas chromatograph (GC) (Agilent 7890, USA) instrument equipped with a Valco PDHID detector (model D-3-I-7890, VICI, USA) and a micro-packed column packed with carbon molecular sieve (Shincarbon ST, 2 m x 1.0 mm i.d.; Restek Chromatography Products, USA). The gas samples are introduced into the GC column by the 6-port switching valve (A6C6UWT, VICI) from the sampling loop to inject a fixed volume of sample (160 µL). Ultra-high-purity helium (UHP) (99.9995%) is used as both the carrier gas and discharge gas. Two heated helium purifiers (HP2 and HPM, VICI, USA) are placed between the cylinder and the flow splitter to remove impurities in the UHP helium and to stabilize the baseline. The helium flow rate is 30 ml/min regulated by a restrictor (30 cc/min 60 psi He, VICI). The constant pressure mode of the carrier gas is set at 90 psi controlled by a pressure control module (PCM, Agilent). The oven temperature is programmed from 308 K (1.5 min) to 553 (ramping at 20 K/min) holding for 3.25 min. Stainless steel tubing is used throughout the thermal reactor and GC's sampling system. All the connectors have been tested for leaks with an electric leak detector. The catalytic reaction bed is enclosed in a heating block (**Figure S5a**) operated at near-atmosphere pressure. Twelve mg of the catalyst is mixed with 23 mg of silica gel (60/80 mesh, Alltech, USA) and then placed inside a glass tube (2 mm ID × 3 mm OD, 100 mm length) with quartz wool plugs at both ends. As the first step, N_2 gas (50 mL/min) was introduced into the reactor bed at RT for one hour to remove moisture in the catalyst, followed by feeding gas of pure CO_2 or $CO_2 - H_2$ mixture (CO_2 : H_2 = 1 : 3) at 20 mL/min to the reaction bed in the temperature ranging from 323 to 573 K. After 30 min at isothermal temperature, gas

products are injected into the analytic column from the sampling loop for GC analysis. The calibration curves for hydrogen, carbon monoxide, methane, ethane, propane are obtained by analyzing five or six different concentrations of corresponding standard gases in the range from 100 to 5000 ppmv (**Figure S6**). To investigate the precision of the analysis, relative standard deviations (RSDs) are calculated from three repeated analyses. The resulting RSDs are between 0.2% and 1.1% (**Table S6**). Accordingly, the detection limits for H_2, CO, CH_4, C_2H_6 and C_3H_8 are 1.67, 0.55, 0.22, 0.16 and 0.22 ppmv, respectively. Note that the curves are not linear and thus more concentrations could be needed to further enhance accuracy if a wider concentration range is desired.

Results and Discussion

Physical Structure Inspections on NiO$_T$-Pd-T NPs

Figure 1 presents the typical high angle annular dark field-STEM (HAADF-STEM) images of (a) NiO$_T$Pd-T and (b) control sample (Pd-T). Based on Z-contrast for HAADF-STEM imaging, the elemental distribution of the NiO$_T$Pd-T can be clearly visualized in **Figure 1a**. For example, the small island showing the highest Z-contrast can be determined as Pd while the majority of the nanoparticles exhibiting lower Z-contrast are Ni/NiO$_T$. Besides, the support representing the lowest Z-contrast among the catalyst is identified as TMOS. Corresponding energy dispersed spectroscopy (EDS) elemental maps in **Figure 1a** confirms that this is the case (more STEM and EDS results are presented in **Figure S1**). Hence, the NiO$_T$Pd-T NPs comprises Pd islands (denoted by yellow arrows) adjacent to both crystalline NiO$_T$ (red arrows) and amorphous NiO$_T$ (green arrow). Denoted by the blue dashed lines, the truncated surfaces with ordered atomic arrangement reveal the low vacancy density in the Pd

nanocluster and is a typical characteristic of the epitaxial crystal growth on a heterogeneous interface. The atomic arrangement is further revealed by HRTEM images and the corresponding line histogram in **Figure S2**. As indicated by the red arrow in **Figure S2a**, a defected surface (red arrow) with distorted lattice fringes (yellow arrow) suggests that Pd atoms are deposited in a rocky surface (with high defect density) upon the formation of Pd island in NiO$_T$Pd-T. Meanwhile, according to the line histogram (**Figure S2c**) of the selected region (across yellow dashed rectangular) in forward Fourier transformation image in **Figure S2b**, the Pd (111) facets possess two sets of inter-planar distances (2.33 Å and 2.20 Å). Such a phenomenon is a typical characteristic in a semi-coherent interface which again proves the formation of an epitaxial structure by stacking the Pd atoms on the NiO$_T$ surface. In contrast, the HAADF-STEM image and EDS maps of Pd-T are shown in **Figure 1b**. The inner part of the Pd nanoparticles shows well-aligned lattice fringes and atomic arrangements, however, the presence of smeared surfaces with highly disordered structures, as indicated by yellow arrows in **Figure 1b**, is the consequence of rapid crystal growth without specific confinements.

X-ray diffraction (XRD) patterns of experimental NCs are compared in **Figure S3** and corresponding structural parameters are summarized in **Table S2**. In **Figure S3**, peaks X, O, A, B, and C are reflection lines from (111) facet of NiO$_T$, (002) facet of carbon nanotube (CNT), and (111), (200), (220) facets of metallic f.c.c. Pd islands, respectively. Compared to those of Pd-CNT, all diffraction lines are shifted to the left by different extents indicating the uneven lattice expansions in the metallic Pd region in NiO$_T$Pd-T. Such an abnormal structure difference is another evidence for the formation of epitaxial structure in the Pd-to-NiO$_T$ interface. Such a scenario is consistently proved by the uneven deposition rate of Pd atoms (average coherent length, D$_{avg}$) on various facets (see **Table S2**) upon crystal growth in NiO$_T$Pd-T as compared to that of Pd-CNT.
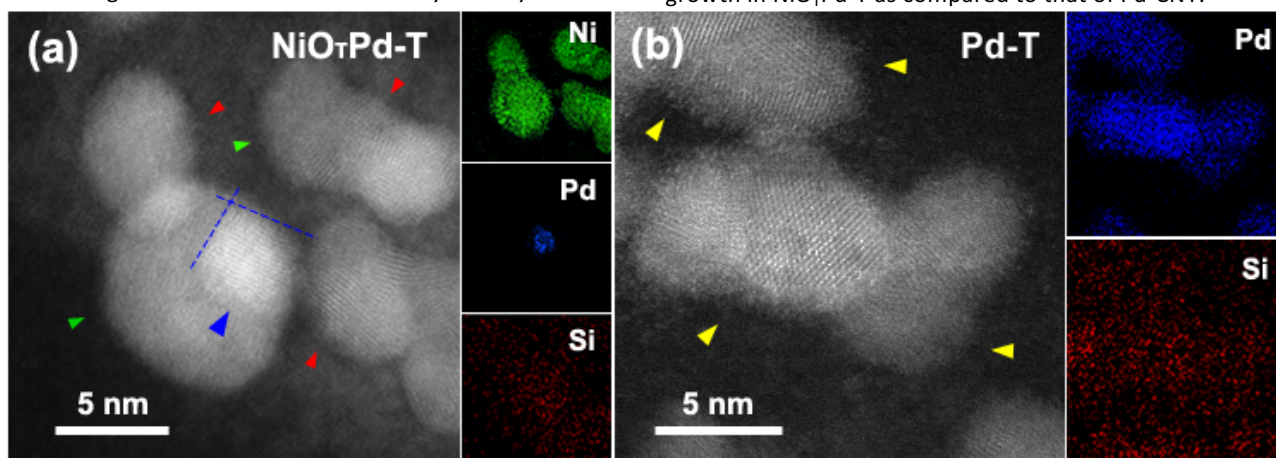

Figure 1. Atomic-scale HAADF-STEM images and corresponding EDS elemental maps of (a) NiO$_T$Pd-T and (b) Pd-T. Blue arrow in (a) indicates the Pd nanoparticle, and red and green arrows highlight the crystalline and amorphous NiO$_T$, respectively. Yellow arrows in (b) highlight the disordered Pd structures.

ARTICLE

The cross-referencing results of XAS analysis at Pd and Ni K-edges complementary rationalize the formation of epitaxial structure between metallic Pd to NiO_T nanocrystals in local structure regimes. **Figure 2a** compares the X-ray absorption near-edge structure (XANES) spectra of experimental (NiO_TPd-T), control (Pd-T), and reference (Pd, NiO_TPd, and Pd foil) samples. In a Pd K-edge XANES spectrum, the presence of two absorption peaks (M and N) accompanied with a deep valley (V) indicating that Pd atoms are metallic state in both Pd and NiO_TPd NCs. In the absorption peak region, the intensity of peak N follows the trend of $h_{N-Pdfoil} > h_{N-Pd} > h_{N-Pd-T} > h_{N-NiO_T Pd-T}$. As compared to the Pd foil spectrum, the suppression of peak N (h_N) with increased intensity in region V can be attributed to the hybridization of 4s/4p by the chemisorption of OH ligand and oxygen in Pd atom both in Pd and NiO_TPd NCs.[19] For the case of Pd NC, the suppression of h_N can be attributed to the formation of silicate in Pd-T. Consequently, further suppression of $h_{N-NiO_T Pd-T}$ can be rationalized by the higher surface to the bulk ratio (i.e., smaller D_{avg}) of NiO_TPd-T as compared to that of Pd-T. The aforementioned scenarios are consistently revealed by the smearing of absorption peaks in the 1st deviation of XANES spectra (inset) and local structure around Pd atoms.

Effects of NiO_T interface and silicate formation on the local structure ordering of Pd region in experimental NCs are elucidated by extended X-ray absorption fine structure (EXAFS) analysis. **Figure 2b** compared the Fourier-transformed EXAFS spectra (i.e., radial structure-function (RSF)) of the experimental NCs and corresponding structural parameters are summarized in **Table S3**. In **Figure 2b**, radial peaks A and B respectively contributed from the interferences of X-rays between Pd-Pd and Pd-O/Pd-Si bond pairs. For Pd NPs, compared to those of Pd foil, the offset of peak A by 0.05 Å with suppression of intensity by 27% indicate the expansion of Pd-Pd bond length (R_{Pd-Pd}) to 2.752 Å and reducing of coordination number around Pd atom (CN_{Pd-Pd}) to 8.09. Those characteristics can be ascribed to the presence of high-density vacancies and local disorder due to the rapid crystal growth of Pd NPs by strong reduction agent ($NaBH_4$). Such a hypothesis can be further rationalized by the substantial smaller CN_{Pd-Pd} of Pd NPs (8.09) as compared to that of an ideal nanoparticle in a close-packed crystal structure and the same D_{avg} of 8.25 nm.[20] For NiO_TPd, compared RSF profile of Pd NPs, the offset of a radial peak by -0.06 Å with suppression of intensity by 34.4% respectively indicate the reduction of R_{Pd-Pd} to 2.746 Å and the decrease of CN_{Pd-Pd} to 6.81. Normally, the

interatomic distance between metallic atoms is increased by decreasing the size of a nanoparticle. Given that hetero-atomic intermix between Ni and Pd atoms (**Table S3**) is absence, the decreasing of R_{Pd-Pd} resembles a lattice compression and consistently proves the formation of an epitaxial structure by stacking metallic Pd structure in NiO_T surface in atomic-scale regime. The RSF profile of experimental samples with silicate decoration (Pd-T and NiO_TPd-T) further confirm the aforementioned scenarios. For Pd-T, compared to RSF of Pd NPs, offset of peak A to the right with suppression of intensity depict the expansion of R_{Pd-Pd} to 2.762 Å with a reduction of CN_{Pd-Pd} to 4.62. Both the two scenarios can be explained by the formation of silicate layer in Pd NPs surface; where oxygen and Si atoms are adsorbed in hollow sides to stretch the distances between Pd atoms. Such a scenario is consistently revealed by formation of direct contact between Pd and silicate in which CN_{Pd-Si} is 2.17 and CN_{Pd-O} is 0.89. For the case of NiO_TPd-T, with a smaller D_{avg} (i.e., the larger surface to bulk ratio) than Pd-T, the stretching of R_{Pd-Pd} and local structure disordering (decreasing of CN_{Pd-Pd}) of NiO_TPd-T is further enhanced (**Table S3**). The local structure around Ni atoms complimentary illustrates the geometric configuration of Pd-T and NiO_TPd-T NCs. **Figure S4** compares Ni K-edge (a) XANES and (b) EXAFS spectra of NiO_T-T and NiO_TPd-T with reference samples (NiO_T NPs, NiO_TPd NPs, and Ni foil). As indicated in **Figure S4a**, Ni atoms in NiO_T and NiO_TPd NPs are staying between metallic and oxide state. After the surface decoration of silicate, the significantly enhanced absorption peak intensity (H_A) and presence of 1s to 3d transition peak (X in inset) depict that metallic Ni atoms are oxidized to local ordered NiO_T with a tetrahedral symmetry around Ni atoms in NiO_T-T and NiO_TPd-T. Such a structural evolution is complimentary proved by the presence of a radial peak in the 2nd coordination shell (**Figure S4b**) suggesting the formation and rearrangement of Ni-O_4 monomers (i.e., the formation of NiO_T). Given that the formation of silicate decoration turns all metallic Ni atoms into oxide, the Pd atoms are deposited as an in-conformal structure in the Ni surface in NiO_TPd-T. Consequently, a high density of local defect is contained in the interface region between Pd and NiO_T which (with high surface energy) facilitates the reduction of Ni-O4 sites and their subsequent local synergetic collaboration with Pd sites in CO_2RR. Details for the structure interpretation from Ni K-edge analysis is provided in ESI and the schematic representation for the nanostructure configuration of experimental samples is demonstrated in **Scheme 1**.
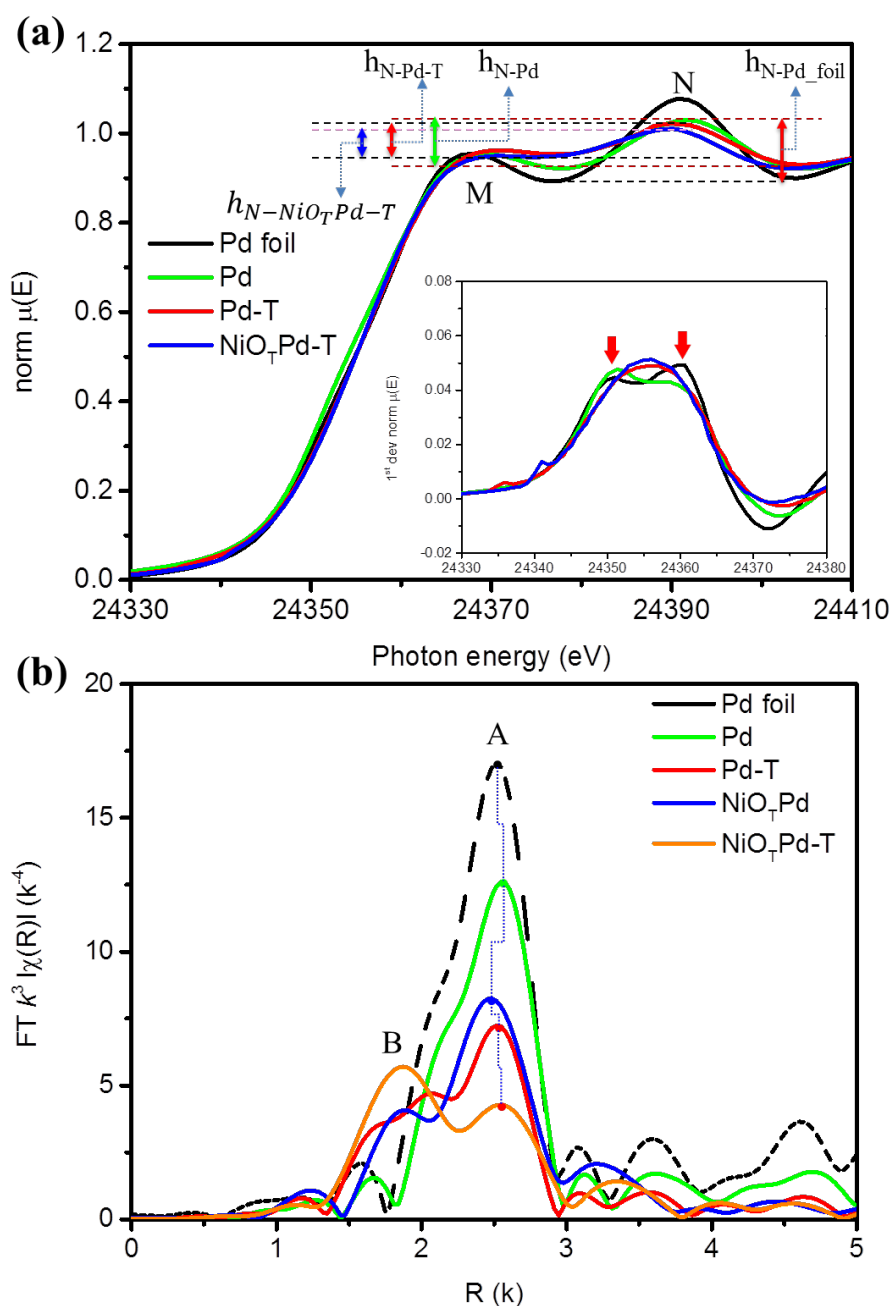
Figure 2. X-ray absorption spectra for Pd K-edge of control samples (Pd foil, Pd NP, and NiO_TPd) and experimental samples (Pd-T and NiO_TPd-T). (a) X-ray absorption near-edge spectra (XANES), (b) Fourier-transformed extended X-ray absorption fine structure (FT-EXAFS). Inset in (a) is the 1st derivative of XANES.

Performance of thermal CO_2RR on NiO_T-T, Pd-T, and NiO_TPd-T NCs

The CO_2 conversion performances for NiO_TPd-T and control samples (NiO_T-T and Pd-T) are analyzed by using Gas Chromatography (GC) with PDHID detectors. The measurement is conducted at normal ambient pressure and the conversion yield is estimated by a concentration unit of mmol per gram catalyst (mmol $g^{-1}_{catalyst}$). The sensitivity of the detection system is ~0.1 ppm and corresponding calibrations are given in the ESI. For clarifying the selectivity of Pd and Ni oxide and interface effects, the production yield of CO and CH_4 in pure CO_2 ambient

are complimentarily discussed. **Figure 3a** compares the CO_2 to CO production yield of all samples in pure CO_2 ambient. Accordingly, the NiO_T-T is inactive to CO_2 below 523K. At 573K the CO concentration of NiO_T-T is 11.8 mmol $g^{-1}_{catalyst}$. For Pd-T, CO concentration is progressively increased from 33.7 mmol $g^{-1}_{catalyst}$ to 87.5 mmol $g^{-1}_{catalyst}$ with temperature from 473K to 573K. Compared to those of NiO_T-T, the lower kick-off temperature (473K) and higher production yield denote the better selectivity and activity of Pd-T on CO_2 to CO conversion. For NiO_TPd-T, the epitaxial structure between Pd and NiO_T surprisingly enhances the CO_2 reduction. In this NC, CO

concentration is increased from 73.2 to 852.6 mmol $g^{-1}_{catalyst}$, which are 2 to 10-fold improved as compared to that of Pd-T, with temperature from 473K to 573K.

Results of CH_4 production yield in a pure CO_2 ambient are compared in **Figure 3b** for verifying the contribution of residual water or CH bonds in CNT to the CO_2RR of experimental samples. Again, the absence of CH_4 proves that NiO_T-T is chemically inert to CO_2 from 323K to 573K. In Pd-T, changes of CH_4 concentration follow the same trend to that of CO and the optimum value is 1.5 mmol $g^{-1}_{catalyst}$ at 573K. For NiO_TPd-T, the CH_4 concentration reaches the optimum value of 3.3 mmol $g^{-1}_{catalyst}$ at 523K and then decreases to 2.7 mmol $g^{-1}_{catalyst}$ by further increasing to 573K.

In the ambient of a CO_2 and H_2 mixture (CO_2:H_2 = 1:3), the CO production yield of NiO_T-T, Pd-T, and NiO_TPd-T NCs is more than 4-folds improved as compared to they are in a pure CO_2 ambient (**Figure 3c**); where the optimum value is 2272.3 mmol $g^{-1}_{catalyst}$ for NiO_T-T, 636.8 mmol $g^{-1}_{catalyst}$ for Pd-T, and **3629.5** mmol $g^{-1}_{catalyst}$ for NiO_TPd-T at 573K. Meanwhile, compared to the case of pure CO_2 ambient (**Table S4**), the kicked off temperature is increased by 50K and can be attributed to the competition of CH_4 formation which leads to the delay of CO_2 to CO conversion in the presence of H_2 on Pd-T NCs. On the contrary, Ni oxide is reduced to metal in the presence of H_2 so that diminishing the kicked off temperature by 50 K – 100 K and increasing the activity of CO_2 reduction on NiO_T-T and NiO_TPd-T NCs. As for CH_4 production (**Figure 3d**), NiO_T-T and NiO_TPd-T hold the same trend to that of CO and gain an optimum value of 1083.2 mmol $g^{-1}_{catalyst}$ and 1905.1 $g^{-1}_{catalyst}$, respectively. On the other hand, the Pd-T shows a fluctuated CH_4 production yield with temperature and hit the best performance of only

92.2 mmol $g^{-1}_{catalyst}$. Such a result can be explained by the strong affinity of H_2 molecule to Pd metal which suppresses the H_2 splitting kinetics to the CH_4 production yield of Pd-T. For clarity, the low-temperature regions of **Figure 3c** and **Figure 3d** are respectively zoomed-in **Figure 3e** and **Figure 3f** (corresponding results are summarized in **Table S4**). As illustrated, the NiO_TPd-T kicks of the CH_4 production at 323 K (while NiO_T-T and Pd-T respectively work at 423 K and 373 K). Given that the as-prepared NiO_TPd-T contains a certain amount of metallic Ni (**Figure 5a**), a spontaneous H_2 splitting to chemisorbed H atom in Ni* site (Ni*-H^{ads}) is expectable. In this event, the local synergetic collaboration between Ni*-H^{ads} and Pd*-CO^{ads} in the epitaxial structured Pd-to-NiO_T interface results in the methanation reaction at near room temperature and will be proved by the in-situ ambient pressure XPS in later sessions. Characteristics in above can be rationalized by cross-referencing results of (1) composition, (2) D_{avg} of Pd crystal, and (3) formation of the epitaxial structure of Pd-to-NiO_T interface of NiO_T-T, Pd-T, and NiO_TPd-T. In the absence of hetero-atomic intermix between Pd and Ni atoms (**Table S3**), the composition effect can be ruled out from all samples. With a D_{avg} of 4.19 nm in Pd region, the specific surface area (i.e., the amount of reaction site) of NiO_TPd-T is 4-folds increased as compared to that of Pd-T (D_{avg} = 8.25 nm). In this event, the improvement of CO_2RR by 10-fold seemly controversial from geometric effects, however, again can be rationalized by the synergetic collaboration between Pd and NiO_T regions in the epitaxial interface. Such exceptional CO_2 to CO and methanation production performances shine light on the extraction of modified fuel by recycling the waste $CO_{2(g)}$ from (even) low temperature fuel cell systems.
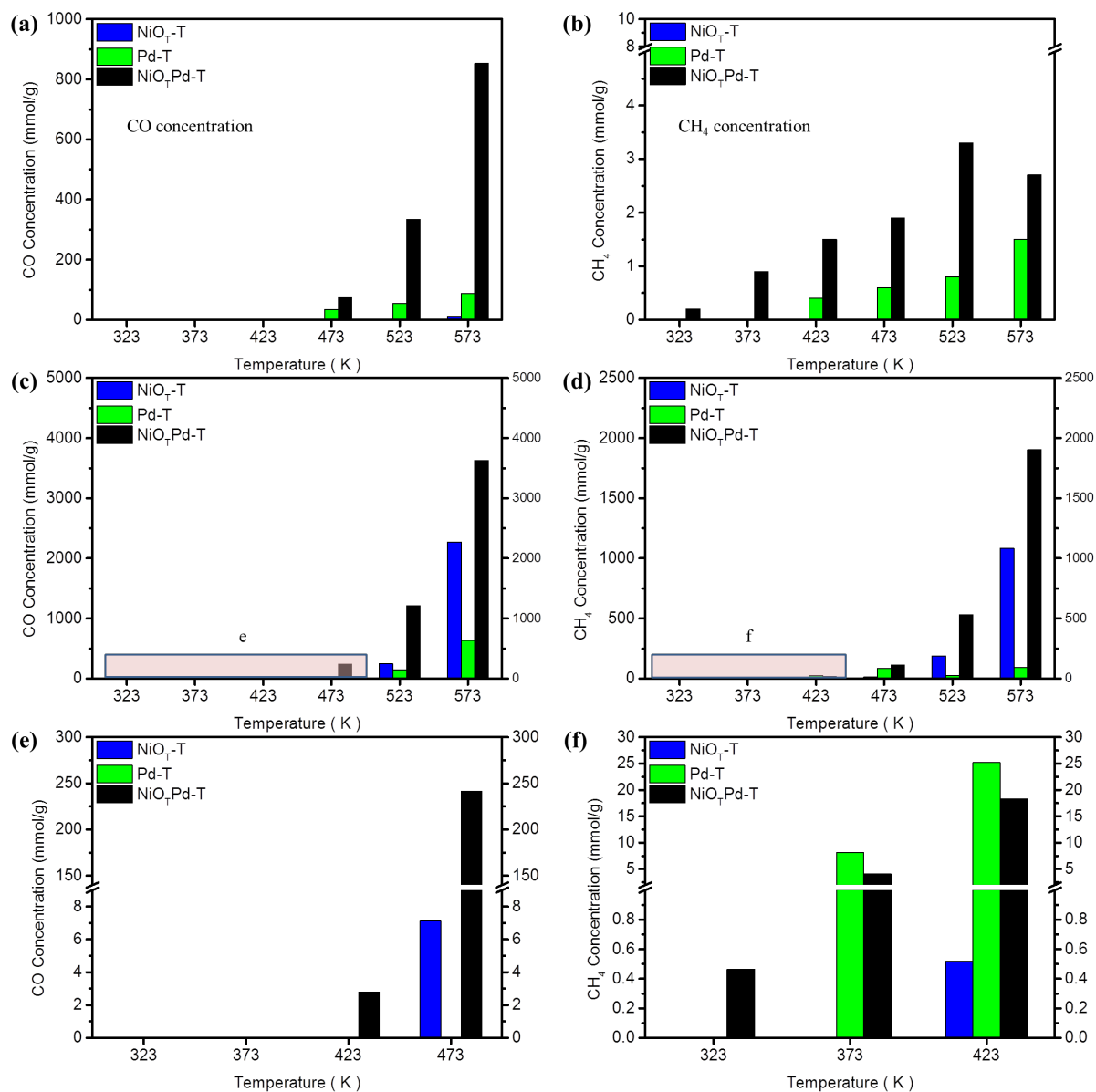
ARTICLE

Figure 3 Gas Chromatography (GC) determined CO_2RR results for the NiO_TPd-T and control samples (NiO_T-T and Pd-T) for (a) CO and (b) CH_4 production yield in pure CO ambient. Results for CO and CH_4 production yield in reaction gas (CO_2+3H_2) are respectively demonstrated in (c) and (d). The regions marked by yellow rectangles e and f are respectively demonstrated in (e) and (f) for clarity. The GC measurements are conducted under a pressure of near 1 atm from 323 K to 573 K and the concentration is normalized by loading of catalysts (mmol/g $_{catalyst}$).

ARTICLE

CO_2RR Mechanisms on NiO_T-T, Pd-T, and NiO_TPd-T NCs

The proposed reaction mechanism is revealed by using in-situ ambient pressure X-ray photoemission spectroscopy (APXPS) at a pressure of 0.11 mbar (near-ambient pressure). For clarifying the reaction coordinates and selectivity of Ni and Pd atoms, results of NiO_T-T and Pd-T are compared as references. **Figure 4a** demonstrates the Ni 2p APXPS spectra of NiO_T-T; where the spectra measured under vacuum and $CO_2 + 3H_2$ mixture at 0.11 mbar (reaction gas) respectively are denoted by Vac and P2. Peaks A (Binding Energy (B.E.) at 852.8, B (B.E. at 856.3), and C (B.E. at 873.4) are corresponding to metallic $Ni^{(0)}$ $2p_{3/2}$, $2p_{3/2}$ for Ni^{n+} (n > 3), and $2p_{1/2}$ for Ni^{n+}, respectively.[21-22] Given that tetrahedral Ni-O sites is confirmed by the presence of a pre-edge peak in Ni K-edge XANES analysis (**Figure S4a**), the presence of high valent state Ni (Ni^{n+}) reveals the formation of amorphous should range ordered NiO_T with a high density of local defects in Ni oxide surface. As indicated, the position and the intensity of all emission peaks remain unchanged, indicating that NiO_T-T is chemical inert to both H_2 and CO_2 molecules till the temperature of 423K. Such a characteristic is expectable due to the prevailing defects in the NiO_T-T surface. At 473K, presence of peak A reveals the formation of metallic Ni^0 and is thermodynamically reasonable via progressive interactions including 1. H_2 adsorption in defect sites ($H_2 + Ni^* \rightarrow Ni^*-H_2^{ads}$), 2. H_2^{ads} splitting into two H atoms ($Ni^*-H_2^{ads} + Ni^* \rightarrow 2Ni^*-H^{ads}$), followed by 3. The interaction between Ni-O (in NiO_T) and Ni^*-H^{ads} into metallic Ni (Ni-O + $Ni^*-H^{ads} \rightarrow Ni^*-OH^{ads} + Ni^{0*}$).[23] At temperatures higher than 473K, with the formation of metallic Ni^0, the suppression of peak A resembles the severe competition between CO_2 and H_2 adsorption followed by the production of high concentration CO and CH_4 consistent with the result of GC analysis (**Figure 3a**) in NiO_T-T. In-situ APXPS spectra of Pd-T at Pd $3d_{5/2}$ are compared in **Figure 4b**. Accordingly, Pd atoms stay in the metallic state at vacuum. In reaction gas, compared to a vacuum state, the binding energy of both peak A and B is increased by 0.2 eV and can be attributed to the contribution of CO adsorption in Pd-T surface.[24] After that, the binding energies are progressively decreased to a value below metallic state and can be attributed to the electron relocation by the strong H_2 molecule affinity in the bulk and chemisorption (poisoning) of CO (CO^{ads}) on the surface Pd atoms with increasing temperature from 323 K to 573 K. Different from the scenarios of NiO_T-T, without the assistance of H atoms, a high contents of reaction sites is occupied by the CO^{ads} resulting in the significant lower CO and CH_4 production yields of Pd-T as compared to that of NiO_T-T (**Figure 3c**). Results of aforementioned APXPS analysis complimentary with GC inspections resemble that the NiO_T and Pd respectively possess a high selectivity to H_2 splitting and CO_2 to CO conversion reactions and corresponding reaction coordinates are demonstrated in **Figure 4c** and **4d**.
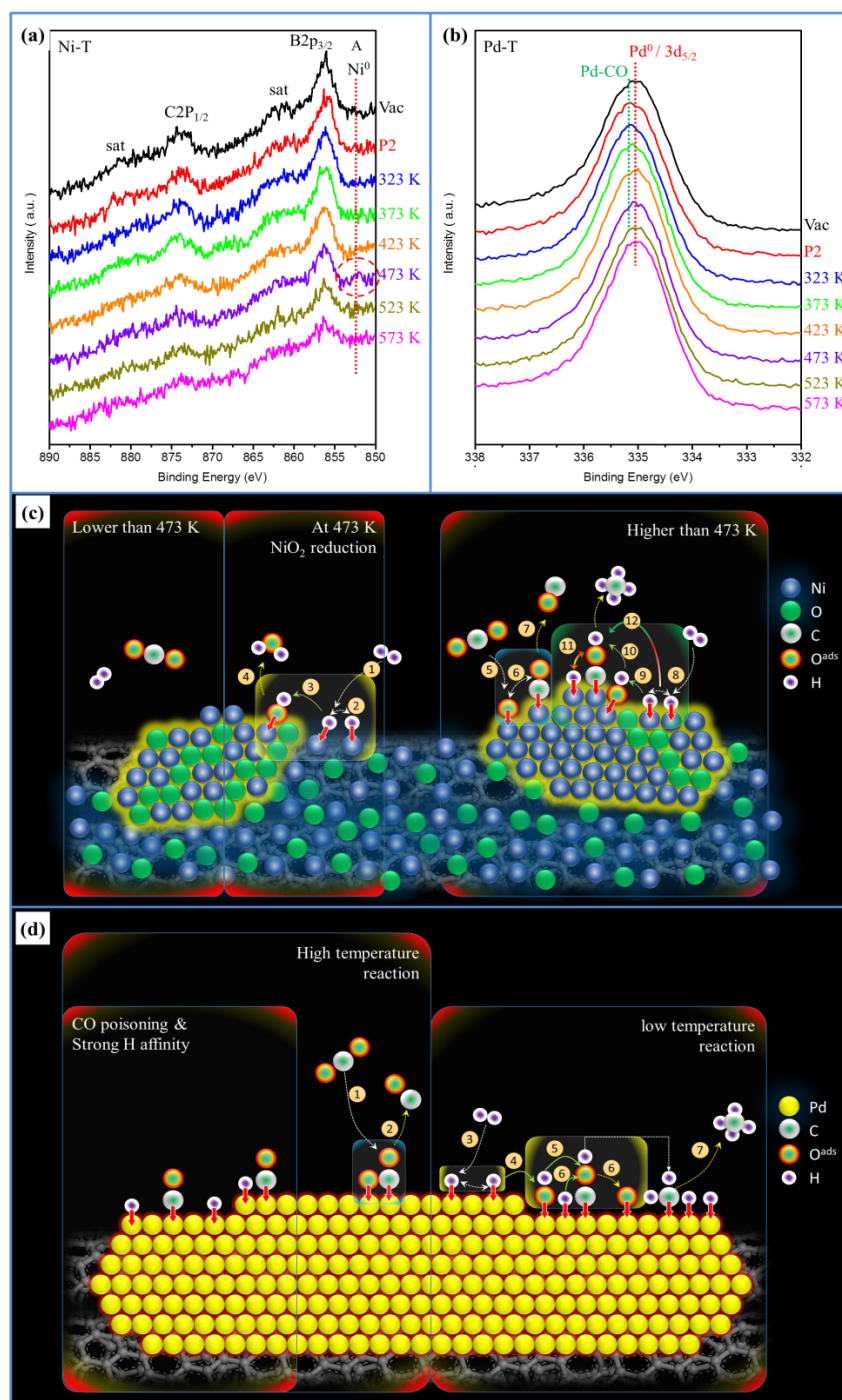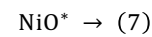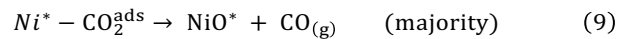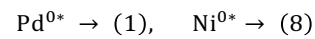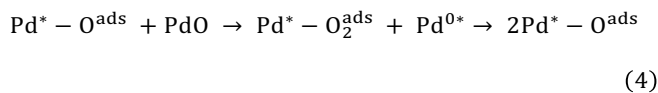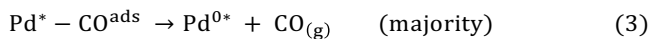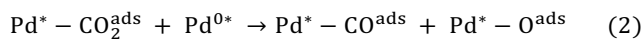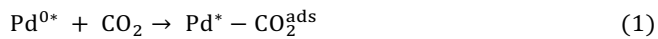
ARTICLE

Figure 4. Ambient pressure XPS spectra of (a) Ni 2p of NiO_T-T and (b) Pd 3d for Pd-T NCs. The corresponding mechanisms on CO_2 to CO and methanation reactions on NiO_T-T and Pd-T are respectively demonstrated in (c) and (d). The proposed reaction coordinates are summarized in Table S5 for NiO_T-T on CO_2RR. For Pd-T, the proposed reaction coordinates are the same as in Table 1 (No. 1-7).

ARTICLE

Figure 5a demonstrates the APXPS spectra in Ni 2p of NiO_TPd-T in pure CO_2 (P1) and reaction gas (P2) at different temperatures. Accordingly, the presence of peak A indicates the co-existence of metallic Ni and high valent state Ni defect sites in the freshly prepared NiO_TPd-T surface (Vac). In P1 ambient, the chemical states of NiO_T-T don't have any significant change from room temperature till 523 K At 573 K, the presence of a weak peak A (metallic Ni^0) resembles rapid desorption of CO^{ads} via a local synergetic collaboration between metallic Pd and Ni atoms in the NiO_T to Pd interface and metallic Ni atoms in defects of NiO_T. By removing CO_2 from reaction chamber (R-V), the intensity of peak A is slightly increased compared to that of Vac suggesting that a considerable amount of NiO_T is reduced to metallic Ni by the CO_2RR at 573 K. Chemical state evolutions of Pd atoms provide complementary evidence for the aforementioned scenarios on Ni atom in P1 ambient. Corresponding APXPS spectra in Pd 3d are compared in **Figure 5b**; where the doublet peaks D and E are the contribution of $3d_{3/2}$ and $3d_{5/2}$ form metallic Pd and the peaks D* and E* are those of Pd oxide. As can be seen in spectrum in Vac state, the metallic Pd and PdO are coexistence in the surface of as-prepared NiO_TPd-T. After introducing CO_2, compared to those of Vac, the progressive suppression of peaks D* and E* with the reduced binding energy (offset of emission peaks to the right) indicate the prevailing CO_2^{ads} in metallic Pd atoms followed by the decomposition of Pd-CO_2^{ads} into Pd-CO^{ads} and Pd-O^{ads} and their interaction to the neighboring Pd oxide with increasing temperature till 573 K. Within these reaction steps, consistently shown in **Figure 5a**, a certain amount of Pd-CO^{ads} will interact with the defect sites of neighboring NiO_T and then increasing the amount of metallic Ni atoms in NiO_TPd-T at 573 K. The scenarios mentioned above can be comprehensively described by following equations:

$$Pd^{0*} + CO_2 \rightarrow Pd^* - CO_2^{ads} \qquad (1)$$

$$Pd^* - CO_2^{ads} + Pd^{0*} \rightarrow Pd^* - CO^{ads} + Pd^* - O^{ads} \qquad (2)$$

$$Pd^* - CO^{ads} \rightarrow Pd^{0*} + CO_{(g)} \qquad \text{(majority)} \qquad (3)$$

$$Pd^* - O^{ads} + PdO \rightarrow Pd^* - O_2^{ads} + Pd^{0*} \rightarrow 2Pd^* - O^{ads}$$

$$(4)$$

$$Pd^* - CO^{ads} + PdO \rightarrow 2Pd^{0*} - CO_{2(g)} \qquad (5)$$

$$Pd^* - CO^{ads} + NiO_T^d \rightarrow Pd^* - CO_2^{ads} + NiO^* \qquad (6)$$

$$Pd^* - CO_2^{ads} \rightarrow (2)$$

$$Pd^* - CO^{ads} + NiO^* \rightarrow Pd^{0*} + Ni^{0*} + CO_{2(g)} \qquad (7)$$

$$Pd^{0*} \rightarrow (1), \quad Ni^{0*} \rightarrow (8)$$

$$Ni^{0*} + CO_2 \rightarrow Ni^* - CO_2^{ads} \qquad (8)$$

$$Ni^* - CO_2^{ads} \rightarrow NiO^* + CO_{(g)} \qquad \text{(majority)} \qquad (9)$$

$$NiO^* \rightarrow (7)$$
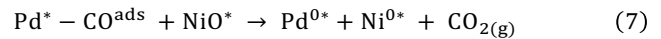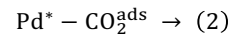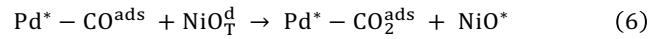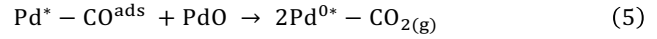
Where eqns (6) and (7) resemble the local synergetic collaboration in the epitaxial interface between Pd and NiO_T regions. Such a collaboration effect increases the metallic Ni and Pd atoms, therefore, resulting in a quantum leap of CO production yield (eqns (9) and (3)) in NiO_TPd-T as compared to both NiO_T-T and Pd-T (**Figure 3a**).

Changes of chemical states on Ni and Pd atoms in the H_2 and CO_2 mixture further elucidate the local synergetic collaboration effects on CO_2RR in NiO_TPd-T. Shown in **Figure 5a**, the progressive decreasing of oxide peaks (B and C) simultaneously with the increasing of Ni^0 intensities illustrate the rapid reduction of NiO_T by increasing temperature from P2 (room temperature) to 573 K. By removing the reaction gas (R-V2), further suppression of oxide peaks (B and C) depicts the removal of CO_2 from Ni^0 surface. For Pd 3d spectra (**Figure 5b**), the binding energies of D and E remaining unchanged indicating the prevailing H_2 molecules (suppression of CO_2^{ads}) in Pd atoms. By increasing temperature from 473 K to 573 K, presence of a shoulder (peak E") with the increasing of binding energy resemble the formation of high contents of CO^{ads} in Pd atoms. In the absence of a chemical shift in Ni atoms and the prevailing metallic Ni atoms (**Figure 5a**), the high contents of CO^{ads} with prevailing metallic state resemble the strong CO_2 affinity with rapid reduction rate on Pd atoms in the NiO_TPd-T at 573 K. After removing the reaction gas and return to room temperature, the binding energy of emission lines is increased by ~0.2 eV which indicates a substantial residual CO_2^{ads} (i.e., the strong affinity and selectivity of CO_2) on Pd atoms in NiO_TPd-T.[24]
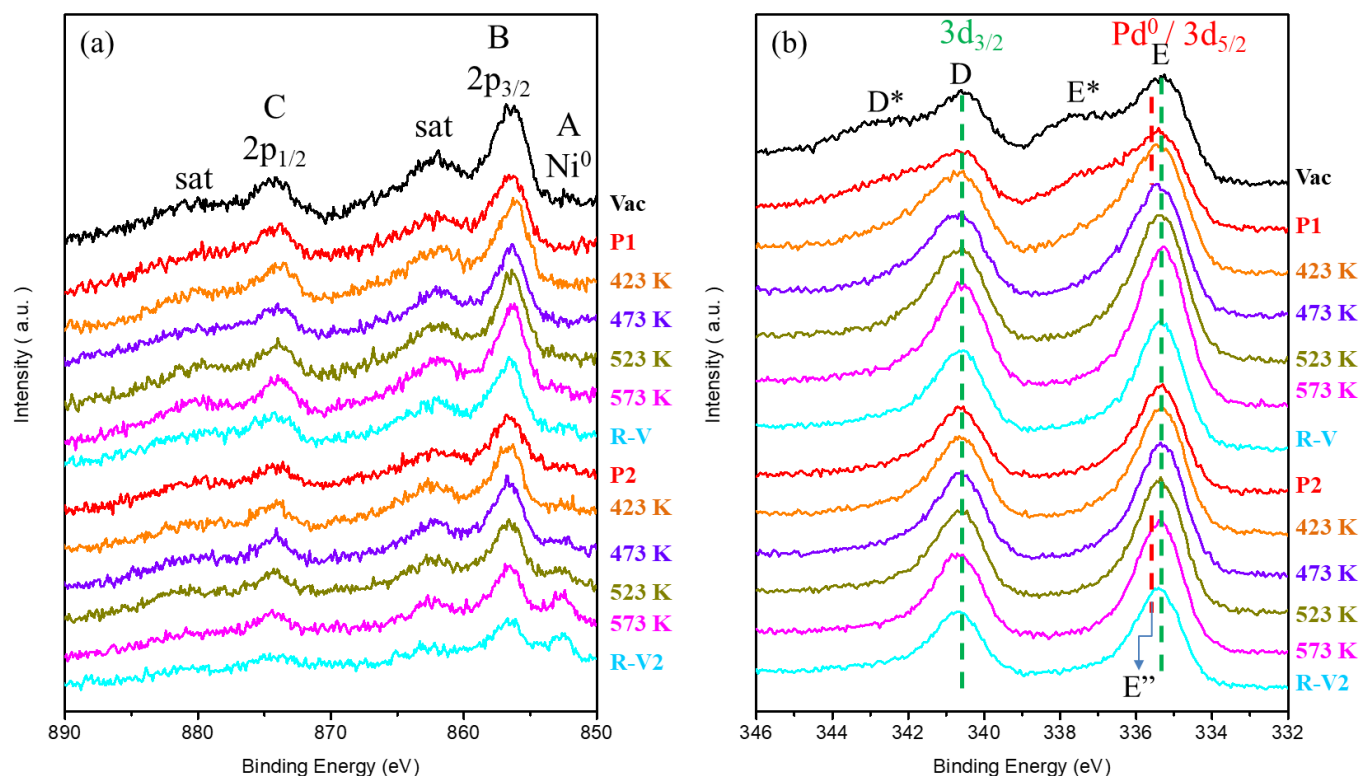
Figure 5. In-situ ambient-pressure X-ray photoelectron spectroscopy (APXPS) spectra of NiO_TPd-T at (a) Ni 2p and (b) Pd 3d regions. The spectra are measured starting from the vacuum (Vac) to ambient of CO_2 in 0.11 mbar at room temperature (P1) and then at the temperature increasing till 573 K. After that, the chamber is vacuumed and cool to room temperature (R-V) then purged by reaction gas of CO_2 and H_2 with the ratio of 1:3 for $CO_2:H_2$ (P2) and heat from 423 K to 573 K.

Results of APXPS analysis at Ni 2p and Pd 3d core level complimentary with the physical structure inspections confirm the local synergetic collaboration in the epitaxial structured interface between NiO_T and Pd regions to the outstanding CO_2RR performance (**Figure 3**) of NiO_TPd-T. Accordingly, Pd and Ni atoms respectively tend to interact with CO_2 and H_2 molecules. There are fourteen reaction coordinates subsequently taking place with the collaboration of reaction sites including Pd, Ni, atoms and defect of NiO_T in the metal-to-metal oxide interface and the corresponding pathways for the CO_2 to CO and methanation reactions are demonstrated in **Scheme 1** and the corresponding coordination loop is summarized in **Table 1**. They are (1) adsorption followed by splitting of CO_2 into chemisorbed CO^{ads} and O^{ads} in metallic Pd^{0*} site ($Pd^{0*} + CO_2 \rightarrow Pd*-CO_2^{ads} + Pd^{0*} \rightarrow Pd*-O^{ads} + Pd*-CO^{ads}$); (2) desorption of CO^{ads} from Pd* site ($Pd*-CO^{ads} \rightarrow Pd^{0*} + CO_{(g)}$); (3) adsorption followed by splitting of H_2 molecule in $2Pd^{0*}$ sites ($Pd^{0*} + H_2 \rightarrow Pd*-H_2^{ads} + Pd^{0*} \rightarrow 2Pd*-H^{ads}$); (4) regeneration of Pd^{0*} sites by the interaction between chemisorbed O^{ads} and H^{ads} in Pd* site ($Pd*-O^{ads} + Pd*-H^{ads} \rightarrow Pd*-OH^{ads} + Pd^{0*}$); (5) formation of chemisorbed formyl (COH^{ads}) by the interaction between chemisorbed CO^{ads} and OH^{ads} in Pd* sites ($Pd*-CO^{ads} + Pd*-OH^{ads} \rightarrow Pd*-COH^{ads} + Pd*-O^{ads}$); (6) transformation of chemisorbed formyl to methylene by interaction with H^{ads} in Pd* sites ($Pd*-COH^{ads} + Pd*-H^{ads} \rightarrow Pd*-CH_2^{ads} + Pd*-O^{ads}$); (7) methanation reaction between chemisorbed methylene and 2H

atoms ($Pd*-CH_2^{ads} + 2Pd*-H^{ads} \rightarrow Pd*-CH_4^{ads} \rightarrow CH_{4(g)} + Pd^{0*}$). The seven reaction coordinates dominate the CO_2RR in the Pd region of NiO_TPd-T. Among them, the first four coordinates (1st to 4th) appear when the temperature below 423 K and the 5th to 7th occur by further increasing temperature till 573 K. (8) Reduction of NiO_T occurs in the 8th coordinate by the interaction between chemisorbed H^{ads} and defect sites of NiO_T ($4Pd*-H^{ads} + NiO_T \rightarrow 4Pd^{0*} + Ni^{0*} + 2H_2O$) and generates high contents of Ni^{0*} sites in the Pd-to-NiO_T interface. (9) In the 9th coordinate, H_2 molecules are adsorbed and then split into H^{ads} in two Ni^{0*} sites ($2Ni^{0*} + H_2 \rightarrow 2Ni*-H^{ads}$). (10) In the presence of high contents of $Ni*-H^{ads}$, (10th step) both reduction of NiO_T ($4Ni*-H^{ads} + NiO_2 \rightarrow 5Ni^{0*} + 2H_2O$) and **[25]** (11) formation of COH^{ads} in the Pd-to-NiO_T interface ($Ni*-OH^{ads} + Pd*-CO^{ads} \rightarrow Ni*-O^{ads} + Pd*-COH^{ads}$) are facilitated. The subsequent reaction coordinates occur in the same region; where the presence of $Ni*-O^{ads}$ facilitates the reduction of NiO_T to the subsequent reduction coordinates. (12) In the 12th step, the COH^{ads} in Pd* sites are transformed into methylene by interacting with H^{ads} in the Ni* sites ($Ni*-H^{ads} + Pd*-COH^{ads} + \rightarrow Ni*-O^{ads} + Pd*-CH_2^{ads}$ and then (13) turned to methane by further interacting with H^{ads} in Ni* sites ($2Ni*-H^{ads} + Pd*-CH_2^{ads} \rightarrow 2Ni^{0*} + Pd*-CH_4^{ads} \rightarrow CH_{4(g)}$) in the 13th step. Notice that, a considerable amount of Ni^{0*} sites appears in the 8th step and could be the main reason for the onset of CH_4 production at 323 K (inset of **Figure 3d**). By further increasing temperature, the reaction kinetics of H_2

splitting to $2H^{ads}$ is facilitated by the presence of Ni^0*. Such a scenario promotes the reduction of NiO_T into Ni^0* in the 10th step. Consequently, the reaction kinetics of 9th to 13th steps is substantially enhanced which rationalizes the quantum leap of CH_4 production yield on NiO_TPd-T by increasing reaction temperature higher than 423 K; (14) In the 14th step, the residual $Ni*-O^{ads}$ in the 11th and 12th steps will interact with $Ni*-H^{ads}$ resulting in the $Ni*-OH^{ads}$ and Ni^0*. The two species will respectively join the 11th and the 9th steps, therefore, turn on the series coordination loop in the two sides of the epitaxial structured Pd-to-NiO_T interface. By adopting the proposed metal-to-metal oxide interface in a single nanoparticle, the synergetic collaboration between Pd and Ni atoms performs the exceptional CO_2 to CO conversion in a pure CO_2 ambient at 473 K and triggers the CH_4 production activity at a surprising temperature near room temperature (323 K). Such exceptional performances shine a light on the development of a modified fuel system by combining the CO_2 recycle catalysts with state-of-the-art fuel cell modules.
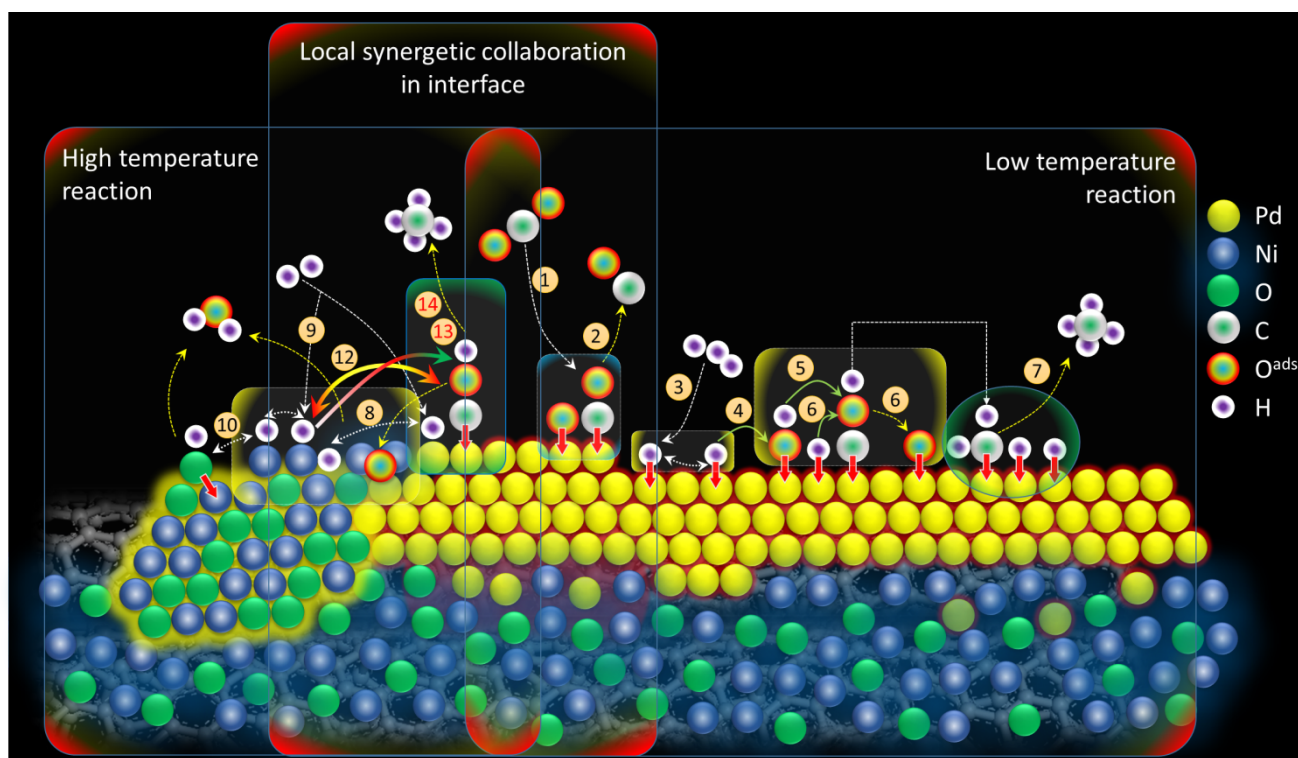
Scheme 1 Schematic representation for the reaction coordinates in the NiO_TPd-T.

Table 1 The proposed reaction coordinates and the corresponding coordination loop for the experimental NiO_TPd-T on CO_2RR.

No.	reaction coordinates	intermediate species	subsequent reaction	Intermediate species	Subsequent reaction	Product
(1)	$Pd0* + CO_2 \rightarrow Pd*-CO_2^{ads} + Pd0* \rightarrow Pd*-CO^{ads} + Pd*-O^{ads}$	$Pd*-CO^{ads}$	(2)	$Pd*-O^{ads}$	(4)	
(2)	$Pd*-CO^{ads} \rightarrow Pd0* + CO_{(g)}$	$Pd0*$	(1)			$CO_{(g)}$
(3)	$Pd0* + H_{2(g)} \rightarrow Pd*-H_2^{ads} + Pd0* \rightarrow 2Pd*-H^{ads}$	$Pd*-H^{ads}$	(4)			
(4)	$Pd*-O^{ads} + Pd*-H^{ads} \rightarrow Pd*-OH^{ads} + Pd0*$	$Pd0*$	(1)	$Pd*-OH^{ads}$	(5)	
(5)	$Pd*-CO^{ads} + Pd*-OH^{ads} \rightarrow Pd*-COH^{ads} + Pd*-O^{ads}$	$Pd*-O^{ads}$	(4)	$Pd*-COH^{ads}$	(6)	
(6)	$Pd*-COH^{ads} + Pd*-H^{ads} \rightarrow Pd*-CH_2^{ads} + Pd*-O^{ads}$	$Pd*-O^{ads}$	(4)	$Pd*-CH_2^{ads}$	(7)	
(7)	$Pd*-CH_2^{ads} + 2Pd*-H^{ads} \rightarrow Pd*-CH_4^{ads} \rightarrow Pd0* + CH_{4(g)}$	$Pd0*$	(1)			$CH_{4(g)}$
(8)	$4Pd*-H^{ads} + NiO_T \rightarrow 4Pd0* + Ni0* + 2H_2O$	$Pd0*$	(1)	$Ni0*$	(9)	
(9)	$2Ni0* + H_{2(g)} \rightarrow 2Ni*-H^{ads}$	$Ni*-H^{ads}$	(10)			
(10)	$4Ni*-H^{ads} + NiO_T \rightarrow 5Ni0* + 2H_2O$	$Ni0*$	(9)			
(11)	$Ni*-OH^{ads} + Pd*-CO^{ads} \rightarrow Ni*-O^{ads} + Pd*-COH^{ads}$	$Ni*-O^{ads}$	(14)	$Pd*-COH^{ads}$	(12)	
(12)	$Ni*-H^{ads} + Pd*-COH^{ads} \rightarrow Ni*-O^{ads} + Pd*-CH_2^{ads}$	$Ni*-O^{ads}$	(14)	$Pd*-CH_2^{ads}$	(7) (13)	
(13)	$2Ni*-H^{ads} + Pd*-CH_2^{ads} \rightarrow 2Ni0* + Pd*-CH_4^{ads} \rightarrow CH_{4(g)}$	$Ni0*$	(9)			$CH_{4(g)}$
(14)	$Ni*-O^{ads} + Ni*-H^{ads} \rightarrow Ni*-OH^{ads} + Ni0*$	$Ni0*$	(9)	$Ni*-OH^{ads}$	(11)	

Conclusions

In this study, we developed a bimetallic NiO_TPd NC with a novel epitaxial structure of metallic Pd nanocluster adjacent to a Ni oxide nanocrystallite with tetrahedral local symmetry (NiO_TPd-T). Our results of GC analyses revealed that the NiO_TPd-T possesses the optimum production yields of 1905.1 mmol $g^{-1}_{catalyst}$ on CH_4 and **3629.5** mmol $g^{-1}_{catalyst}$ on CO at 573 K, respectively. Those results are more than 10-fold improved as compared to those of Pd NC (Pd-T) synthesized by using the same method without adjacent to NiO_T interface. Results of physical structure inspections and in-situ APXPS analysis indicate that such an outstanding performance is accounted for the local synergetic collaboration between Pd and Ni atoms in the interface. In this region, Pd and Ni atoms respectively tend to form CO^{ads} and H^{ads} bond which facilitates the reduction of NiO_T to increase the amount of metallic Ni sites for H^{ads} and thus promote the methanation reaction by sequentially incorporating the formyl ligand formation followed by the hydrogenation with the assistance of prevailing Ni-H^{ads}. Of most importance to the best of our knowledge with such a novel Pd-to-NiO_T epitaxial structure, the experimental NC performs the highest CH_4 production yield among existing catalysts with the same loading, composition, and different configurations. Besides, such a low-temperature methanation performance rationalizes the possibility on the development of modified fuel with thermal energy recycle by combining the properly designed system with proposed NiO_TPd-T catalyst and (even low temperature) fuel cell modules.

Conflicts of interest

There are no conflicts to declare.

Acknowledgements

Notes and references

1. M. A. Arellano-Trevino, N. Kanani, C. W. Jeong-Potter and R. J. Farrauto, *Chemical Engineering Journal*, 2019, **375**, 8.
2. M. A. A. Aziz, A. A. Jalil, S. Triwahyono and A. Ahmad, *Green Chemistry*, 2015, **17**, 2647-2663.
3. Q. Liu, L. Liao, Z. Liu and X. Dong, *Chinese Journal of Chemical Engineering*, 2011, **19**, 434-438.
4. I. Luisetto, S. Tuti and E. Di Bartolomeo, *International Journal of Hydrogen Energy*, 2012, **37**, 15992-15999.
5. J. J. Tan, J. M. Wang, Z. Y. Zhang, Z. Ma, L. H. Wang and Y. Liu, *Applied Surface Science*, 2019, **481**, 1538-1548.
6. A. H. Fakeeha, S. O. Kasim, A. A. Ibrahim, A. E. Abasaeed and A. S. Al-Fatesh, *Materials*, 2019, **12**, 1777.
7. F. Starr, in *Structural Alloys for Power Plants*, eds. A. Shirzadi and S. Jackson, Woodhead Publishing, 2014, DOI: https://doi.org/10.1533/9780857097552.1.36, pp. 36-68.
8. L. Falbo, C. G. Visconti, L. Lietti and J. Szanyi, *Applied Catalysis B-Environmental*, 2019, **256**, 12.
9. H. Kierzkowska-Pawlale, J. Tyczkowski, J. Balcerzak and P. Tracz, *Catalysis Today*, 2019, **337**, 162-170.
10. W. H. Li, Y. Liu, M. C. Mu, F. S. Ding, Z. M. Liu, X. W. Guo and C. S. Song, *Applied Catalysis B-Environmental*, 2019, **254**, 531-540.

11. C. F. Liang, Z. M. Ye, D. H. Dong, S. Zhang, Q. Liu, G. Z. Chen, C. C. Li, Y. Wang and X. Hu, *Fuel*, 2019, **254**, 18.
12. A. Alarcon, J. Guilera, J. A. Diaz and T. Andreu, *Fuel Processing Technology*, 2019, **193**, 114-122.
13. X. Y. Huang, P. Wang, Z. C. Zhang, S. N. Zhang, X. L. Du, Q. Y. Bi and F. D. Huang, *New Journal of Chemistry*, 2019, **43**, 13217-13224.
14. W. L. Vrijburg, E. Moioli, W. Chen, M. Zhang, B. J. P. Terlingen, B. Zijlstra, I. A. W. Filot, A. Zuttel, E. A. Pidko and E. J. M. Hensen, *Acs Catalysis*, 2019, **9**, 7823-7839.
15. J. Liu, C. Li, F. Wang, S. He, H. Chen, Y. Zhao, M. Wei, D. G. Evans and X. Duan, *Catalysis Science & Technology*, 2013, **3**, 2627-2633.
16. J. B. Branco, P. E. Brito and A. C. Ferreira, *Chemical Engineering Journal*, 2020, **380**, 122465.
17. F. Hu, S. Tong, K. Lu, C.-M. Chen, F.-Y. Su, J. Zhou, Z.-H. Lu, X. Wang, G. Feng and R. Zhang, *Journal of CO2 Utilization*, 2019, **34**, 676-687.
18. A. Bermejo-Lopez, B. Pereda-Ayo, J. A. Gonzalez-Marcos and J. R. Gonzalez-Velasco, *Applied Catalysis B-Environmental*, 2019, **256**, 11.
19. W. Barrett, J. Shen, Y. Hu, R. E. Hayes, R. W. J. Scott and N. Semagina, 2020, **12**, 944-952.
20. Y. Zhuang, J. P. Chou, H. Y. T. Chen, Y. Y. Hsu, C. W. Hu, A. Hu and T. Y. Chen, *Sustainable Energy & Fuels*, 2018, **2**, 946-957.
21. M. C. Biesinger, B. P. Payne, A. P. Grosvenor, L. W. M. Lau, A. R. Gerson and R. S. C. Smart, *Applied Surface Science*, 2011, **257**, 2717-2730.
22. H. Ali-Löytty, M. W. Louie, M. R. Singh, L. Li, H. G. Sanchez Casalongue, H. Ogasawara, E. J. Crumlin, Z. Liu, A. T. Bell, A. Nilsson and D. Friebel, *The Journal of Physical Chemistry C*, 2016, **120**, 2247-2253.
23. I. Sreedhar, Y. Varun, S. A. Singh, A. Venugopal and B. M. Reddy, *Catalysis Science & Technology*, 2019, **9**, 4478-4504.
24. M. Borasio, 2006.
25. Q. Jeangros, T. W. Hansen, J. B. Wagner, C. D. Damsgaard, R. E. Dunin-Borkowski, C. Hebert, J. Van Herle and A. Hessler-Wyser, *Journal of Materials Science*, 2013, **48**, 2893-2907.
26. R. G. El-Sharkawy, *Colloids and Surfaces A: Physicochemical and Engineering Aspects*, 2019, **583**, 123871.
27. C.-H. Wang, S.-T. Chang, S.-Y. Chen and Y.-W. Yang, 2019, **205**